Flexural and Cracking Behavior of Clay Plates under Bending
Insights from Novel Tests and New Suction Parameters

Cengiz, Cihan; Su, Yao Yang; Zwanenburg, Cor

DOI
10.1520/GTJ20250033

Publication date
2026

Document Version
Final published version

Published in
Geotechnical Testing Journal

Geotechnical Testing Journal

Cihan Cengiz,[1] Yao Yang Su,[2] and Cor Zwanenburg[2,3]

DOI: 10.1520/GTJ20250033

Flexural and Cracking Behavior of Clay Plates under Bending: Insights from Novel Tests and New Suction Parameters

Geotechnical Testing Journal

doi:10.1520/GTJ20250033 available online at go.astm.org/pubs

Cihan Cengiz,[1] Yao Yang Su,[2] and Cor Zwanenburg[2,3]

Flexural and Cracking Behavior of Clay Plates under Bending: Insights from Novel Tests and New Suction Parameters

Manuscript received March 4, 2025; accepted for publication September 8, 2025; published online October 22, 2025.

[1] Deltares, Boussinesqweg 1, 2629 HV Delft, the Netherlands (Corresponding author), e-mail: cihan.cengiz@deltares.nl, https://orcid.org/0000-0002-9475-8124

[2] Deltares, Boussinesqweg 1, 2629 HV Delft, the Netherlands

[3] Delft University of Technology, Stevinweg 1, 2628 CN Delft, the Netherlands

Reference

C. Cengiz, Y. Y. Su, and C. Zwanenburg, "Flexural and Cracking Behavior of Clay Plates under Bending: Insights from Novel Tests and New Suction Parameters," *Geotechnical Testing Journal* https://doi.org/10.1520/GTJ20250033

ABSTRACT

This study investigates the flexural and cracking behavior of clay plates under pure bending conditions through a novel experimental framework. The test methodology overcomes limitations of traditional beam flexure and burst tests by employing an inflatable membrane to apply a uniform bending pressure while continuously supporting self-weight of the specimen. Kaolin clay plates of varying thicknesses were prepared by slurry consolidation and subjected to bending tests in an instrumented assembly. The bending stresses and moments, pore water pressures, and displacement of the surface were measured with conventional sensors. Additionally, the deformations of the specimens were captured with a three-dimensional scanner to evaluate the curvature and cracking patterns. Beyond the innovative experimental setup, this study also sheds light into the suction regime in clays subjected to flexure and sets forth novel pore water pressure parameters, which correlate well with the cracking tendencies of the clay material. A distinct curvature threshold is defined, and it is observed that the clay material's crack opening tendencies are influenced by the suction regime in the specimen. Beyond the novel insights offered in this study, the normalized bending resistances yielded from the tests correlate well with existing research.

Keywords

clay bending, clay cracking, curvature, suction

Introduction

Bending and cracking resistance of clay materials are of importance in a wide range of infrastructure assets such as clay cap barriers for landfills (Camp, Gourc, and Ple 2010; Plé et al. 2012; Divya, Viswanadham, and Gourc 2017), hazardous waste containment

(Gourc et al. 2010), uplift of cover layers in dikes (Van, Koelewijn, and Barends 2005; van der Krogt, Schweckendiek, and Kok 2021; Zwanenburg et al. 2024), embankment dam stability (Leonards and Narain 1963), and slope stability (Zhang et al. 2012; Jamalinia, Vardon, and Steele-Dunne 2020). In addition to affecting the mechanical properties, cracks also provide preferential flow paths to fluids, thus significantly increasing the hydraulic conductivity of the material over its uncracked value (Thusyanthan et al. 2007).

In geotechnical engineering practice, clay is used as a naturally occurring construction material, and in most cases, its use is mandated by the type of structure or the local geologic conditions. For instance, in dike engineering, particularly in lowland or deltaic regions, the clay cover layer is often part of the natural stratification and cannot be readily replaced due to functional or environmental constraints (Cengiz et al. 2024). The bending and cracking behavior of the clay cover layer is of utmost importance in dike engineering as it might cause catastrophic failure of the dike in delta regions under elevated hydraulic loading conditions as illustrated in **figure 1**. **Figure 1** pictorially depicts a high-water event scenario where the flexural resistance of the clay cover layer is of critical importance for stability of the dike. High water heads might seep through the permeable sand and cause uplift deformations in the clay in which case the bending resistance of the clay becomes critical. In **figure 1**, the dike body is situated on top of a naturally occurring clay layer which is referred to as the natural foundation clay layer by the International Levee Handbook (CIRIA 2013). Throughout this manuscript, this layer is termed as the cover layer.

Furthermore, it is well established that the frequency and severity of extreme environmental events, such as droughts, extreme precipitation events, and flash floods, are increasing rapidly (Vardon 2015; Vu and Mishra 2019; Gössling et al. 2023). The emergence of these climatic stressors increase the relevance of the cracking and bending behavior of clays layers in relation to the stability of flood defense infrastructure. Therefore, there is a need to develop a further understanding of flexural behavior of clays to ensure the resilience of critical infrastructure and the long-term sustainability and efficiency of using clay as a naturally occurring construction material.

Despite the significance of bending and cracking behavior of clays in many engineering applications, there are only few experimental studies available in the literature, which shed light on the issue. The topic is mostly investigated within the context of landfill clay cap performance with the main concern being the bending of the clay cap due to differential settlements of the contained waste. Camp, Plé, and Gourc (2009) have developed an element-scale testing method to assess the bending and cracking behavior on landfill covers made out of clay materials. In follow-up studies, Camp, Gourc, and Ple (2010) and Gourc et al. (2010) reported on the deformation behavior of clay caps based on field and centrifuge scale modelling activities. Plé et al. (2012) has made use of the

FIG. 1 Uplift of the clay cover layer.

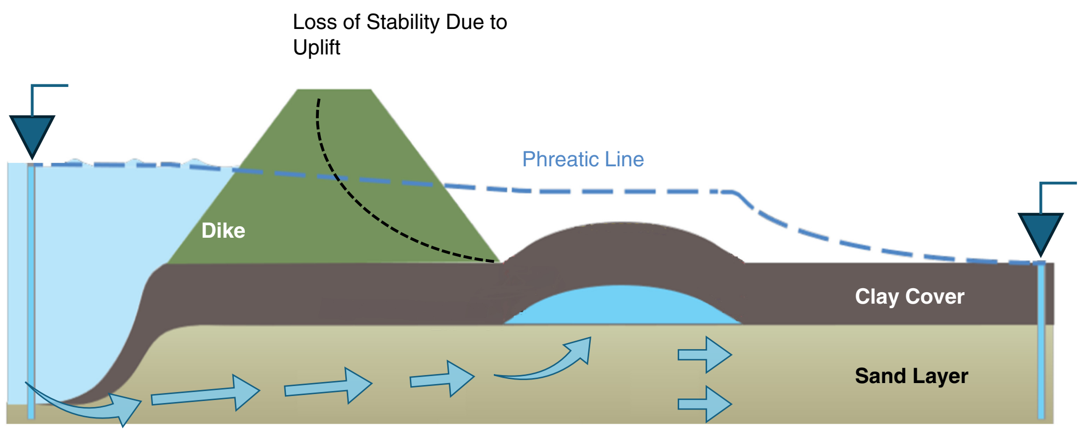

FIG. 2

Schematic representation of the three basic fracture modes in a rectangular block: mode I (opening/tensile), mode II (sliding/in-plane shear), and mode III (tearing/out-of-plane shear).

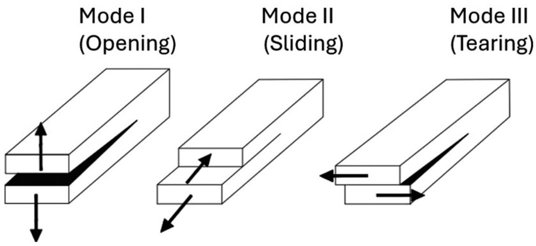

field work conducted by Gourc et al. (2010) and also investigated the flexural behavior by way of conducting small-scale bending tests and finite element modelling. Li et al. (2022) used distributed strain sensing type measurement techniques to assess the flexure behavior of compacted clay beams. Furthermore, Tang et al. (2015) and Li et al. (2019) have investigated the tensile strength of compacted clayey soils by a series of tensile tests.

In fracture mechanics, distinction is made between three modes of failure as depicted in **figure 2**. In geotechnical context, crack formation is generally initiated bending moments, which leads to vertically oriented cracks as in mode I (tensile opening where tensile stresses are horizontally oriented). Mode II type failure is also relevant for clays where in-plane shear is the dominant fracture mode. From a macroscopic point of view, the failure mode for fracture initiation is considered to be either tensile or shear failure (Marchi, Gottardi, and Soga 2014). However, as explained by Marchi, Gottardi, and Soga (2014), there are opposing views on the fracture initiation of clays: one group of researchers (Bjerrum et al. 1972; Decker and Clemence 1981; Jaworski, Duncan, and Seed 1981; Fukushima 1986; Lo and Kaniaru 1990; Andersen et al. 1994) considers tensile failure as the mode for fracture initiation, whereas another group (Mori and Tamura 1987; Panah and Yanagisawa 1989; Atkinson 1994; Zervos, Papanastasiou, and Vardoulakis 2008) suggests that shear failure is the cause. Despite the lack of consensus, the dominant fracture mechanism in clays may depend on a combination of material properties, boundary conditions, and loading characteristics. Beyond the fracture initiation mechanism associated with clay material failure, there are no unified methods of testing the bending capacity of clay materials as highlighted by the studies undertaken by Wang et al. (2007) and Wang et al. (2020).

In order to address the lack of a unified testing method, this study introduces a novel testing framework that is designed to subject circular clay plates to pure bending conditions while continuously supporting self-weight of the clay specimen throughout the testing process. Most of the available literature on clay bending makes use of prismatically shaped clay beams to carry out bending tests with three- or four-point bending setups. In such cases, the self-weight of the clay causes unintended deformations of the specimen. In other cases where burst type apparatus is used (Gourc et al. 2010), there are shortcomings associated with the stress concentrations in the corners of the trapezoidal loading plate, which artificially prescribe the bending and cracking initiation locations. Consequently, in such setups, the clay is not allowed to bend under its own natural deformation tendencies as dictated by its inherent strength and stiffness. Moreover, the curvature applied to the specimen is limited and localized in the above-mentioned studies and as a result large deformation response of the material is not studied.

The test method introduced herein overcomes the shortcomings of previous methods and may pave the way for a unified testing procedure. The experimental setup features an inflatable membrane to continually support and induce a dome-shaped displacement on the clay plate specimens. This method minimizes unintended deformation during testing and yields a geometrically controlled loading configuration that allows for first-order interpretation using classical strength of materials theory. The experimental setup also benefited from instrumentation and surface scanning techniques, which allowed for monitoring of the response of the clay in terms of displacements and pore water pressures as well as yielding information on crack development and propagation during the tests. Furthermore, this study introduces innovative negative pore water pressure (suction) parameters, which provide an enhanced understanding of how pore water pressure regime drives cracking in clays during bending. These parameters include root mean square suction, cumulative suction, and cumulative absolute suction change, and they are designed to quantify suction variability and cumulative effects to offer novel insights into the interplay between suction and cracking behavior. Additionally, use of kaolin clay allows for reproducibility and comparison of the results with existing studies as this commercially available material is well-characterized and widely used in the existing literature. Overall, this study not only provides a new testing framework that alleviates the limitations of the existing testing methods but also presents novel insights into the bending and cracking behavior of clay materials.

Experimental Methodology

In bending tests of soils, minimizing the influence of the self-weight of the specimen is a widely recognized challenge (Wang et al. 2007) and several studies reported improvements on the classical 3-point bending for testing of single-edge cracked soil beams by employing support plates under the beam (Hallett and Newson 2001) or using additional bearings under the crack (Chandler 1984). In a more recent study, Aliha, Kouchaki, and Haghighatpour (2023) have demonstrated the design of a new specimen preparation technique called "modified edge-notched disc bend" to study mixed mode fracture problems. However, this method is applicable to materials with substantial stiffness and strength and consequently it does not provide a good solution for the testing of soft materials.

TESTING ASSEMBLY

In order to mitigate the effects of the self-weight in the determination of the bending capacity of clay materials, the current experimental assembly was designed to provide continuous support for the clay plate. With the use of the inflatable membrane with a thickness of 3 mm and a tensile stiffness of 1,200 kPa, the specimen was supported from the bottom, with the motivation to ensure that the applied loading on the specimen closely resembles uniform loading on a plate and pure bending conditions are imposed. As depicted in figure 3, the membrane is clamped down between the flat flange at the bottom of the assembly and the circular steel ring, which laterally confines the clay material. The steel ring with a clear diameter of 284 mm is uniformly torqued down from all sides of the assembly, which creates a watertight seal for clay consolidation. The clay slurry is consolidated directly on top of the membrane. Once consolidation is completed, bending tests take place. For bending tests, water from the mains supply is flowed through an instrumented channel in the bottom plate, resulting in a spherical inflation

FIG. 3

A sketch of the experimental assembly used (all units are in millimeters).

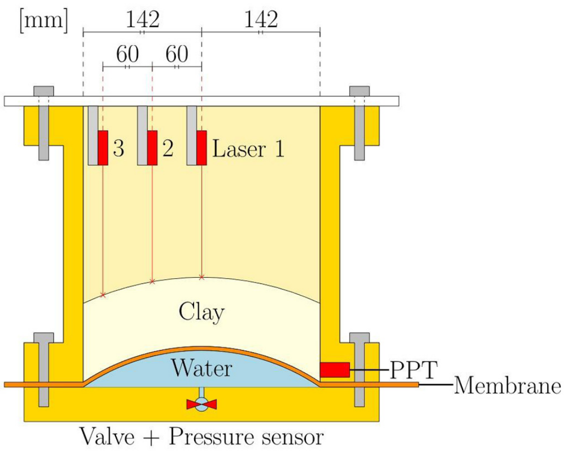

of the membrane due to the water pressure. The amount of flow and thus pressure under the membrane is controlled using a valve. The testing assembly described herein is fundamentally different than that of the classical 3-point-bending setups (Liu et al. 2023; Tang et al. 2024) used for materials with substantial flexure capacity or the 4-point-bending method elaborated in Thusyanthan et al. (2007) for clays.

In natural dike environments, the clay cover may interface directly with a subsurface water layer, particularly in deltaic regions. In the present setup, the supporting membrane replaces this with a mechanically controlled interface that allows the upward pressure to be imposed in a stable and repeatable manner. Although a water layer could offer hydraulic realism, it would introduce additional uncertainties due to fluid-structure interaction, uncontrolled pore pressure development, and potential remobilization of the clay into suspension. The membrane, in contrast, provides a mechanically clean and geometrically controlled boundary with negligible tensile stiffness. This enables the study of flexural behavior in isolation, without the confounding effects of hydraulic feedback or material degradation.

SPECIMEN PREPARATION

The clay used in the experimental program is a commercially available kaolin clay (KD 2000, supplied by Sibelco GmbH). The material is well characterized due to its frequent use in a number of laboratory tests both in the available literature (Smith 1993; Rossato, Ninis, and Jardine 1994; Lau 2015) and in the institute that the authors are affiliated with (Zwanenburg et al. 2023). The kaolin has a liquid limit of 66 %, a plastic limit of 27 %, and a saturated permeability in the order of 10^{-9} m/s (Al-Tabbaa and Wood 1987). The specific gravity of the material is 2.63.

The clay slurry is prepared at 1.5 times its liquid limit, which corresponds to a water content of 99 %. This water content was selected to ensure thorough hydration and minimize the occurrence of lumps within the clay slurry. The selection of this water content level for slurry preparation is well documented in the literature (Murugesan and Rajagopal 2010; Frikha, Bouassida, and Canou 2013; Cengiz and Güler 2018). Precalculated amounts of distilled water and clay powder are used, with the clay powder gradually added and gently mixed by mass to avoid introducing air bubbles into the slurry. Once the clay slurry achieved a uniform consistency, it was added to the testing assembly by gravitational flow and spread evenly over the membrane. A layer of filter geosynthetic is applied on top of the clay to minimize the amount of slurry leakage during the early phases of consolidation. The top flange, which applies the overburden stress over the clay, is fitted with a tube for drainage of excess water. The consolidation stress was applied with a hydraulic actuator controlled by a feedback loop. By allowing the consolidation to occur directly within the testing assembly, a good connection between the clay plate to the side walls of the assembly was ascertained. During the consolidation phase, a laser displacement sensor is used to monitor the amount of settlement of the clay. The clay is consolidated to a target stress of 180 kPa. This stress level was selected so as to ascertain that the residual strength of the clay plates would be in strength range typically encountered in field applications in the Netherlands. In the event that the loading plate did not advance further, the final phase of the consolidation was completed under displacement control where the actuator advanced at a rate of 0.1 N/s to achieve the precalculated settlement.

INSTRUMENTATION AND SURFACE SCANNING

The test setup is instrumented with a single pore pressure transducer (StrainSense EPB-PW-7BS, maximum range 700 kPa) located along, but not protruding from, the edge of the clay plate, which measures the pore pressure during consolidation and during testing. An additional pressure transducer is mounted to the water supply channel to measure the water pressure applied underneath the membrane. The height of the clay plate during bending tests is monitored using three radially spaced laser displacement sensors, one of which was located at the center of the specimen. The laser displacement sensors are secured to a crossbar for easy and consistent mounting and removal.

The ease of laser displacement sensor removal allows an unobstructed surface scan to be performed using the EinScan HX three-dimensional (3D) scanner for every 10 mm of displacement increment as measured by the

FIG. 4 Overlaid cross-sectional profiles of the 44-mm-thick clay specimen at various deformation levels. Point-to-point (C2C) absolute distances are visualized (all in millimeters). The color scale indicates deformation magnitude.

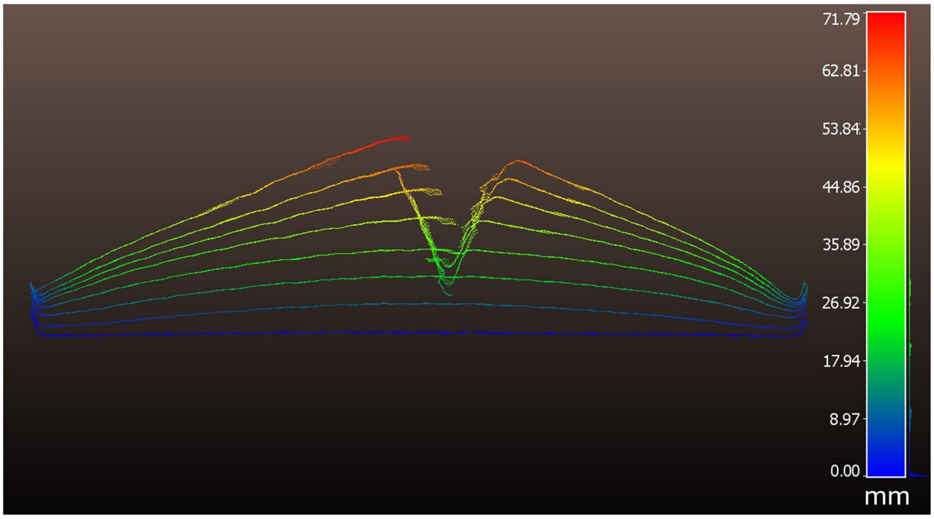

central laser displacement sensor (laser 1 in fig. 3). The surface scans are made with a resolution of ±0.05 mm and the output per scan is retained as a point cloud. An example cross-section acquired from the 44-mm-thick specimen depicting the evolution of deformations and cracking is illustrated in figure 4. The point clouds acquired from each displacement level were aligned using reference markers placed on the topmost flange of the assembly. The point cloud data are used to monitor the evolution of cracking and curvature of the specimens.

TESTING PROCEDURE

The bending stresses are applied to the specimens by way of supplying water pressure below the flexible membrane shown in figure 3. In order to account for the bending effort absorbed by the membrane, a membrane correction is applied by considering a superposition approach. The pressure-displacement curves for the membrane alone and membrane-clay system are discretized and the stress required to mobilize the membrane is removed from the measured values. Figure 5 illustrates an example plot where the method of membrane correction is demonstrated (continuous lines represent the corrected bending stress applied to the clay and numbers following the legend entries show which laser displacement sensor recorded the displacements). Table 1 illustrates the test matrix where the thickness, water content, torvane resistance, and initial pore water pressure of all specimens tested can be seen. Upon completion of each test, a total of three water content measurements were taken from the clay material for water content determination. Additionally, torvane tests were also performed to determine the shear strength of the clay after testing.

Results

EXPERIMENTAL OBSERVATIONS: SENSOR AND IMAGE DATA ANALYSIS

Figure 6 outlines typical results acquired by sensor measurements where test 5 is used as an example case. Figure 6*A* illustrates the controlled loading stages where peaks in inlet pressure increases are followed by plateaus where the system is allowed to stabilize with stress redistribution as evidenced by the changes in pore water pressure (fig. 6*E*). The progressive deformation pattern observed in the clay and membrane system is characterized by a steep initial increase in the stress levels, which indicates a stiff response for lower deformation levels as seen in figure 6*B*. As the deformations increase, the system behaves more plastically and the opening of cracks

FIG. 5

An example plot of the membrane correction applied to test 3 (t = 31 mm).

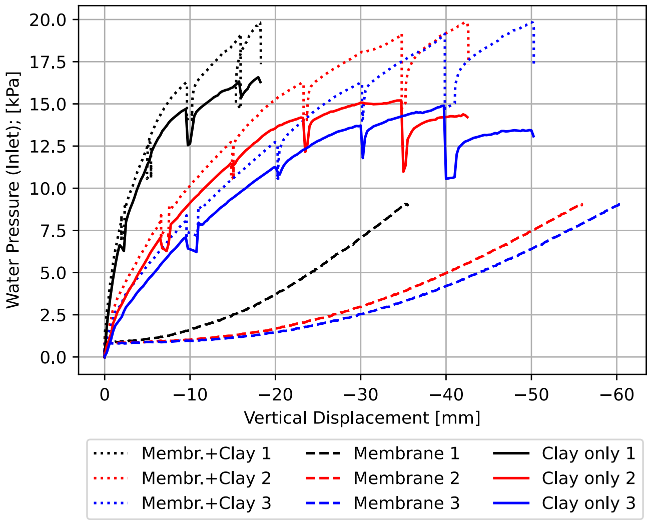

TABLE 1

Test matrix sorted according to the clay thickness

Test Number	Thickness, mm	Water Content, %	Torvane, kPa	Initial PWP, kPa
1	24	43	11.67	0.45
2	28	46.3	8.02	−7.07
3	31	41.2	13.85	−19.06
4	44	44.7	10.2	−18.82
5	54	41.2	16.76	−20.10
6	57	42.9	10.93	−24.08
7	65	43.7	12.75	−23.61
8	75	44.9	12.57	−17.52
9	83	44.2	11.66	−35.87
10	95	42.5	19.32	−32.77

Note: PWP = pore water pressure.

also contributes to the flattening of the resistance curves. The seemingly large differences between laser displacement sensor readings are due to the respective locations of the sensors where laser 1 measures the apex or the largest displacement of the protruding sphere. Laser displacement sensors 2 and 3 are placed closer to the boundary where vertical deformation is limited. By making use of the superposition principle explained above (see fig. 5), figure 6*D* illustrates the nonlinear deformation versus bending stress graph for clay plate only where a clear transition from elastic to plastic bending regime can be seen. Due to the membrane correction applied, figure 6*D* shows the so-called corrected bending resistance. Figure 6*E* illustrates the evolution of the pore water pressure within the clay over time where large fluctuations are observed. These fluctuations might be indicative of transient hydraulic responses, such as drainage, cracking, and localized pore water pressure increases. Figure 6*F* shows the pore water pressure regime as a function of the applied inlet pressure. It is thought that the point of crack initiation is marked by a change of trend of the inlet pressure versus pore water pressure graph, which occurs at an inlet pressure of 15 kPa, which is indicated by a blue arrow. The opening of the crack might alleviate the suction stress and cause an overall reduction in the measured suction response. These aspects will be elaborated in greater detail in the following discussion.

FIG. 6 Individual plots illustrating key aspects of the bursting test analysis for a clay thickness of 57 mm. (*A*) Time versus inlet pressure and (*B*) pressure versus displacement (clay + membrane), highlighting the combined deformation characteristics. (*C*) Time versus displacement, (*D*) pressure versus displacement (clay only), (*E*) time versus pore water pressure, and (*F*) inlet pressure versus pore water pressure.

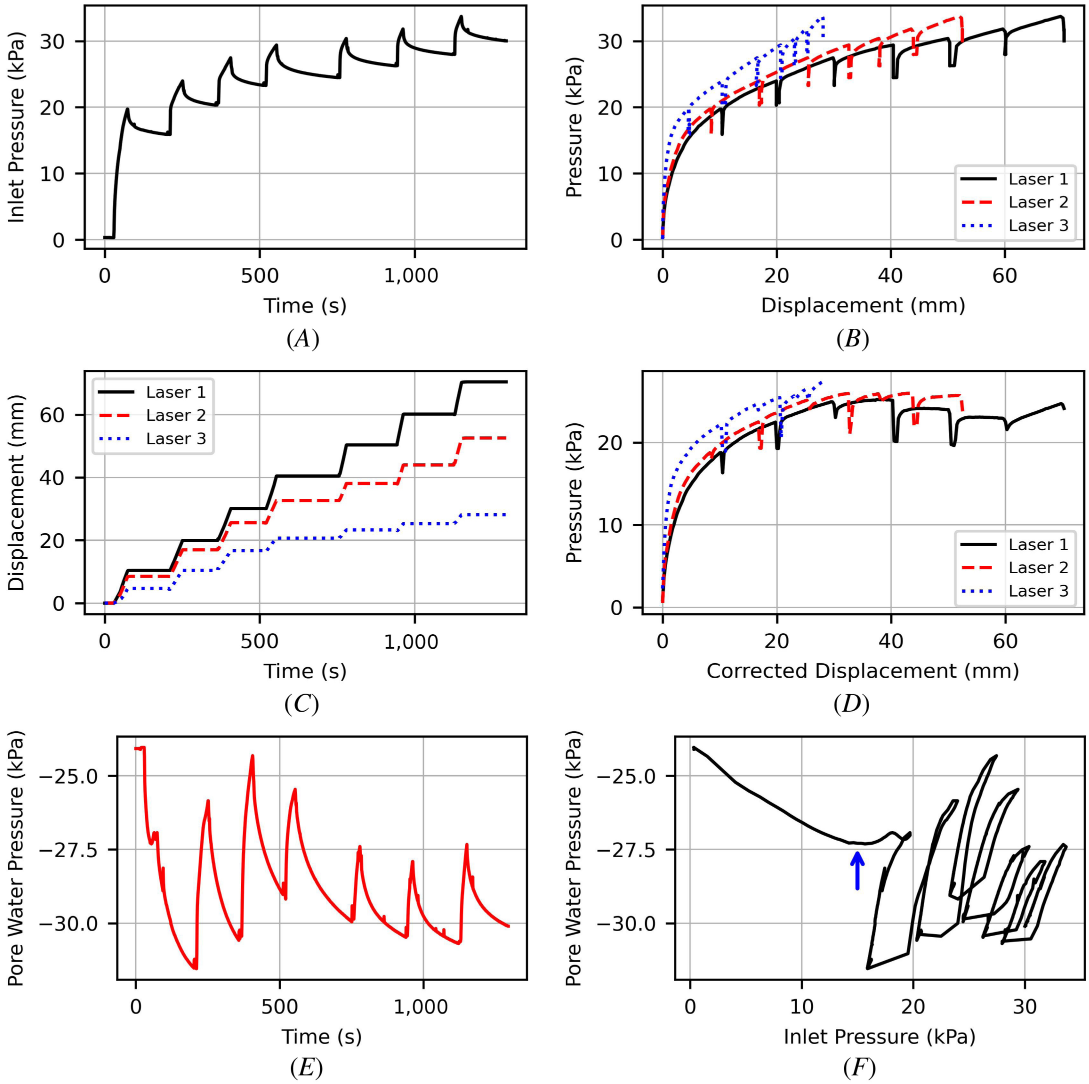

Beyond hard sensor measurements, the experimental campaign made extensive use of image data to quantify the curvature and cracking behavior of the specimens. The image analysis of the burst tests relied on the point cloud data generated by the 3D scanning method prescribed above. For each deformation level, the outer rim of the point cloud was filtered out by applying a radial distance threshold from the center of the scanned geometry. In particular, a 20-mm-wide outer rim was eliminated to mitigate the effects of noise in the scan data stemming from reflections and irregular points acquired on the inner side of the steel cells. Once the basic filtering of the point cloud was completed, random sample consensus or RANSAC algorithm (Fischler and Bolles 1981) was used for shape detection in a two-step manner. In the first step, a plane is used to compute the height map of the deformed shape. An example case of the outcomes of this first step is illustrated in **figure 7** where a photograph of the deformed clay specimen and the cloud-to-mesh vertical distances are seen in **figure 7A** and **figure 7B**, respectively.

FIG. 7 Images of the 44-mm-thick specimen during testing: (*A*) photograph showing the deformed and cracked shape of the specimen and (*B*) height map illustrating the deformation profile.

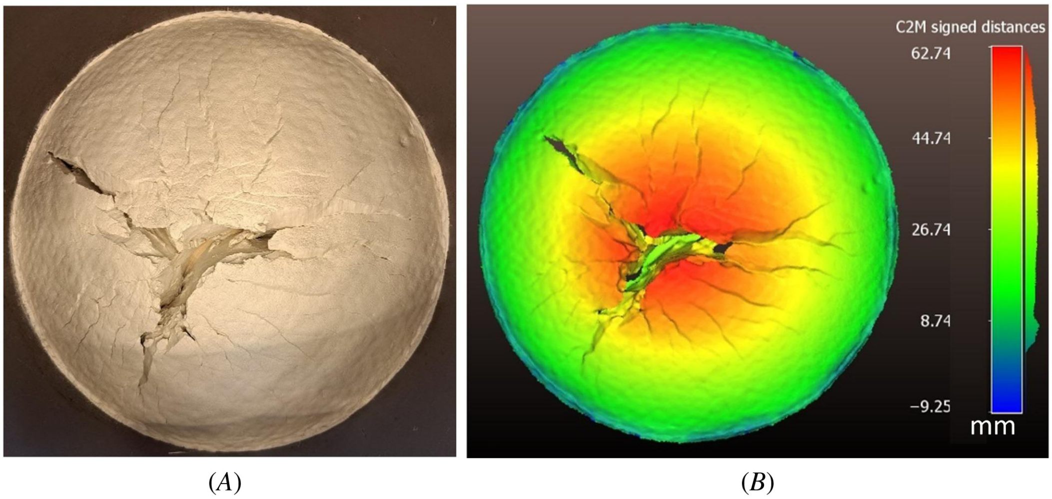

In the second step of the image analysis, a sphere was fitted to the deformed shape using the RANSAC algorithm where the minimum number of support points were prescribed to be at least half of the points in the entire point cloud population with an overlooking probability of 0.001. The minimum number of support points was selected as the half of the population to ensure that sphere fitting would be robust and representative of the entire population. The rather small overlooking probability of 0.001 was chosen to minimize the rejection of a well-fitting sphere (Chum and Matas 2008). The fitting of the sphere also makes use of a maximum distance of 1.4 mm from the primitive sphere feature to account for the irregularities of the clay surface as well as the scanning resolution limitations. This threshold was defined based on previous experience from preliminary testing where smaller values excluded valid points and larger values incorporated noise into the dataset. Although exact quantification of error margins was not the primary focus of this analysis, sensitivity checks using known curved surfaces and processing of acquired data indicate that the cracked percentage estimates are robust within a ±1–2 % margin, which is primarily limited by scanner resolution and mesh fidelity.

Figure 8 illustrates a fitted sphere to the deformed geometry and as an illustrative case where the fitting applied to a 44-mm-thick clay specimen is shown. As a result of the above-prescribed fitting procedure, the point

FIG. 8

Example of a fitted sphere generated using the RANSAC algorithm for curvature calculation, applied to the deformed surface of the 44-mm-thick clay specimen. Sphere radius: 294 mm. All measurements are in millimeters.

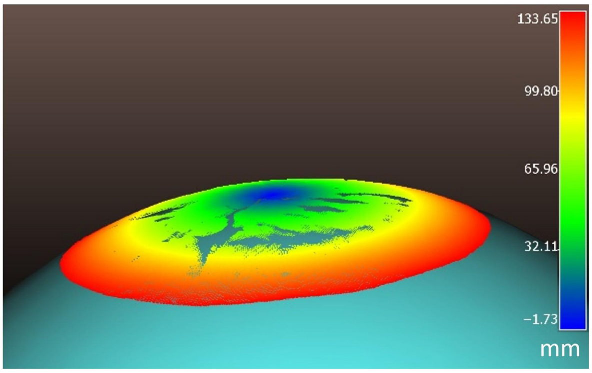

FIG. 9 Height maps of the 44 mm thick clay plate. Panels (*A*, *C*, *E*) show the intact clay surface; panels (*B*, *D*, *F*) show the corresponding residuals. Deformation levels are 40 mm for (*A*, *B*), 50 mm for (*C*, *D*), and 60 mm for (*E*, *F*).

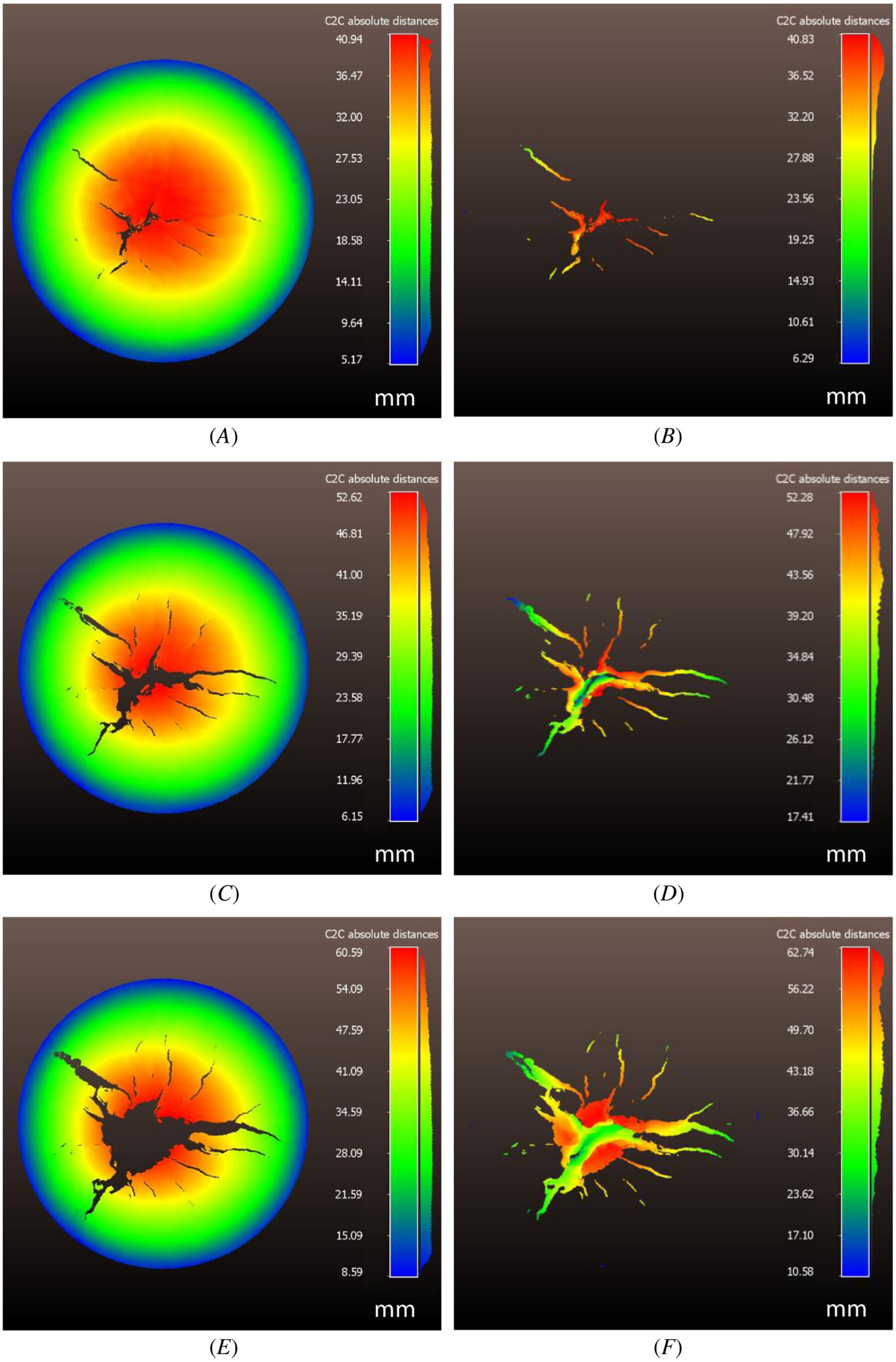

cloud is divided into two clusters and the points belonging to the sphere fitting are deemed as a part of the uncracked clay portion and the remaining points are marked as a part of the crack network. Here it is assumed that deviations from the spherical geometry primarily correspond to crack openings, which are not captured by the smooth sphere geometry. Following the separation of the point cloud, the surface areas of the separated parts are calculated to come up with estimates of the cracked percentage of the clay surface. Specifically, the point clouds were converted into meshes using triangulation and the combined surface area of the triangles was calculated. **Figure 9** illustrates the separated point clouds of the curved plates and the remaining crack networks for various displacement levels for 44-mm-thick specimen.

RESISTANCE TO BENDING

Figure 10*A* illustrates the peak corrected bending resistance (σ_{corr}, membrane correction) for each clay plate at displacement levels ranging from 5 to 80 mm. σ_{corr} is the applied external bending load on the specimen, and it does not consider the internal changes in the specimen such as the change in pore water pressure regime. The marker colors in **figure 10** in general signify different displacement values where marker colors progressively change from purple (low displacement) to yellow (high displacement). **Figure 10*A*** shows that the bending stress increases with increasing clay thickness. Similarly, **figure 10*B*** shows the evolution of pore water pressures at

FIG. 10

(*A*) Corrected bending stress versus clay thickness, (*B*) pore water pressure versus clay thickness.

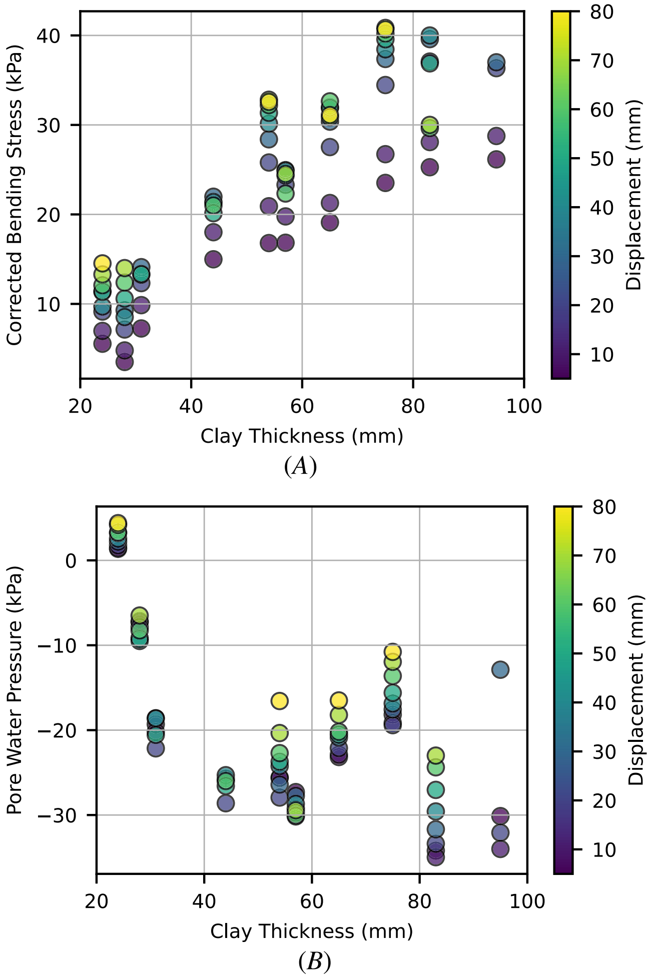

different displacement levels for all clay plates tested. The 24-mm-thick specimen was deliberately designed not to have a large suction pressure imparted on the clay at the end of consolidation. In **figure 10*B***, it is seen that for thinner clay layers, the amplitude of the negative pore water pressure or suction tends to be less than that of thicker layers. It is also observed that on average, the thicker clay layers possess higher suction values at the onset of bending tests, but these values tend to drop sharply as the tests progress.

Figure 11*A* illustrates the relationship between clay thickness and net bending stress. The net bending stress (σ_{net}) is defined as the sum of the corrected bending stress (σ_{corr}), the absolute value of the pore water pressure (|PWP|), and a lateral friction term. The lateral friction term is used to account for the reduction in bending effort, which is caused by friction (or adhesion) between clay plate and inner walls of the steel cell. The magnitude of this adhesion is related with the shear strength of the clay itself, which is known to be lower than the clay's inherent cohesion value (Tsubakihara and Kishida 1993; Tsubakihara, Kishida, and Nishiyama 1993). Therefore, a lower-bound shear strength value, as acquired by torvane testing at the end of the test, is used to estimate the friction. It is thought that the large strains encountered by the clay during the test would reduce the shear strength of the clay to justify this assumption. Finally net bending stress is defined in the following manner:

FIG. 11

Plots of net bending stress with (*A*) initial and (*B*) incremental suction corrections.

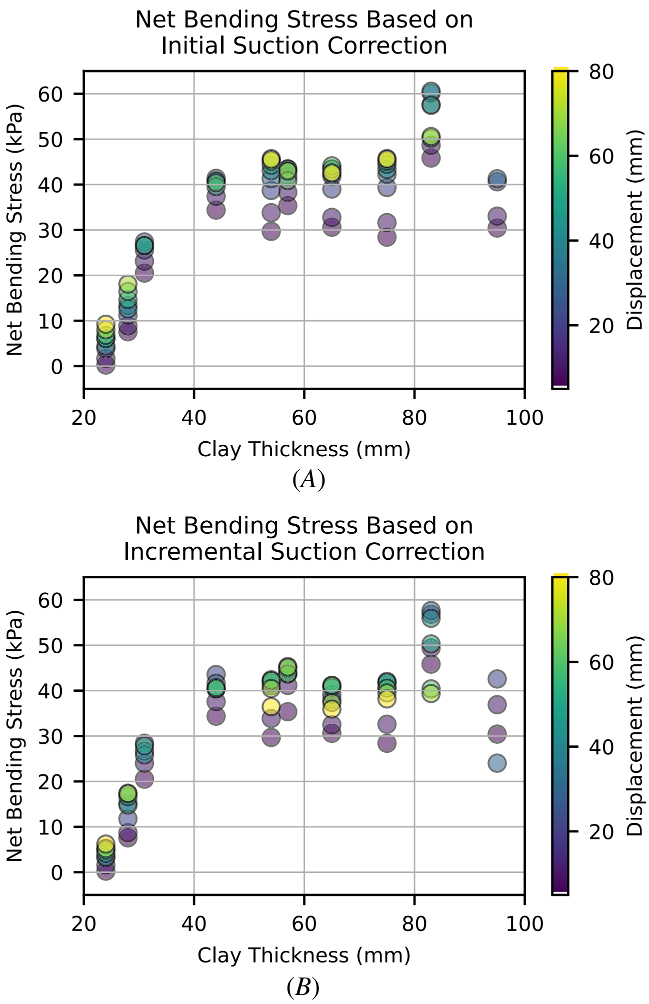

$$\sigma_{net} = \sigma_{corr} + |PWP| - \frac{F_{interface}}{A_{plate}} \tag{1}$$

where $F_{interface}$ is described as $A_{per} \cdot \tau_{torvane}$, which is a multiplication of the peripheral area of the specimen with the measured shear strength of the clay at the end of the test by torvane testing. A_{plate} is the planar area of the clay plates, which is assumed to be constant for all specimens. It should be noted that the |PWP| term uses the initial suction pressures of the specimen, which are tabulated in **Table 1**. A similar assumption has been made by Thusyanthan et al. (2007), and for comparison purposes, this is also considered in the present analysis. Although initial suction values are useful, since the tests span over a large displacement range, it could also be argued that the initial stress-state in the specimen does not immediately affect the response of the clay during the entire duration of the test. With this in mind, **figure 11*B*** illustrates net bending stress calculated with the incremental suction values at each loading increment rather than the initial suction. Although the overall values of bending resistance are lower in **figure 11*B*** due to relaxation of pore water pressures in thicker specimens, a slight increase is observed for thinner specimens. In general, the net bending stress necessitated to bend clay plates increase with increasing plate thickness. Here, it is also important to note that the variability in net bending stress also increases with clay thickness, which might be an indication that thicker clays exhibit more complex stress responses. These complex response patterns might also include the spatial variability of the lateral friction between the clay plate and the inner part of the steel cells. This observation stems from the deformed geometry of the 83- and 95-mm-thick clay plates where the tests were prematurely terminated due to "tumbling" of the specimen, which means excessive rotation of the clay block.

Figure 12 illustrates a comparative plot of the results acquired in the present study and Thusyanthan et al. (2007) where four-point bending tests were performed on kaolin clay beams with a square cross-section of 80 by 80 mm and length of 320 mm. In **figure 12**, the abscissa and ordinate of the graph shows the initial suction stress s_i and net bending stress σ_{net} both of which are normalized by consolidation stress s_o. The marker sizes are increased to indicate increasing displacement levels. Despite the differences in experimental methods and material properties, a good agreement between the results presented by Thusyanthan et al. (2007) and the present study is observed. Thusyanthan et al. (2007) has used consolidation stresses of 297 and 148 kPa for type A and B specimens, respectively. The red continuous line is introduced by the aforementioned study, and it is approximated as the geometric mean of the consolidation stress and initial suction stress with an added fitting parameter and expressed as $-(0.45 \pm 0.15) \times \sqrt{s_o \cdot s_i}$. Thus, the red dotted lines show the error bounds of ±33 %. The best

FIG. 12

Comparative plots of normalized bending stress between Thusyanthan et al. (2007) and the present study.

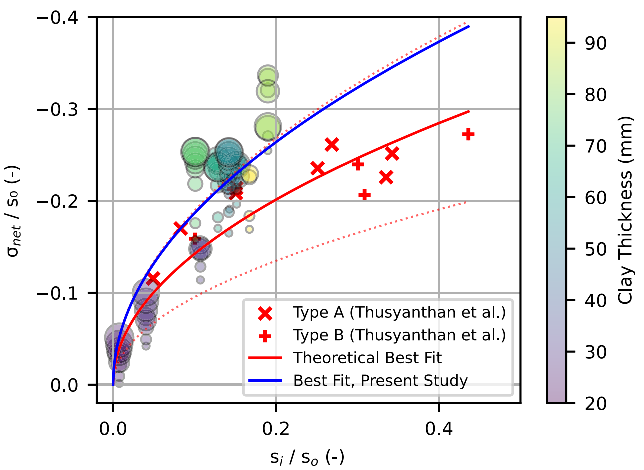

fit line for the present dataset is defined in a similar way with a fitting parameter of −0.59 with $-0.59 \times \sqrt{s_o \cdot s_i}$. It should be noted that for small displacement values, almost all of the data points emanating from the present study stay within the error bounds defined by Thusyanthan et al. (2007). It is thought that the large deformation testing allowed by the present setup introduced the remainder of the variance at large displacements. The relative goodness of fit observed between the two studies is also indicative of the validity of the adhesion correction (see equation (1)) described above. It should be noted that such a correction was not needed in the 4-point bending tests as the specimen was tested 'in-air' devoid of friction effects.

PORE WATER PRESSURES–SUCTION

Figures 10 and **11** demonstrate the influence of suction on clay plate bending response, warranting a deeper investigation. **Figure 13** illustrates the suction regime during the course of the tests. **Figure 13*A*** shows the starting point of negative pore water pressures (suction) for all specimens as well as depicting the evolution of suction. Moreover, detailed information on the pore water pressure regimes can be found in **Table 2**, where measured and derived suction parameters are tabulated. In **figure 13**, increasing marker size indicates increasing displacement levels, and it is seen that the suction trends change with deformations. Here, it is seen that the amplitude of the pore water pressure for thicker specimens vary appreciably throughout the course of the test. The large variance is

FIG. 13

(*A*) Change in pore water pressure versus measured pore water pressure, and (*B*) change in pore water pressure versus clay thickness. In both plots, marker size increases with increasing displacement level.

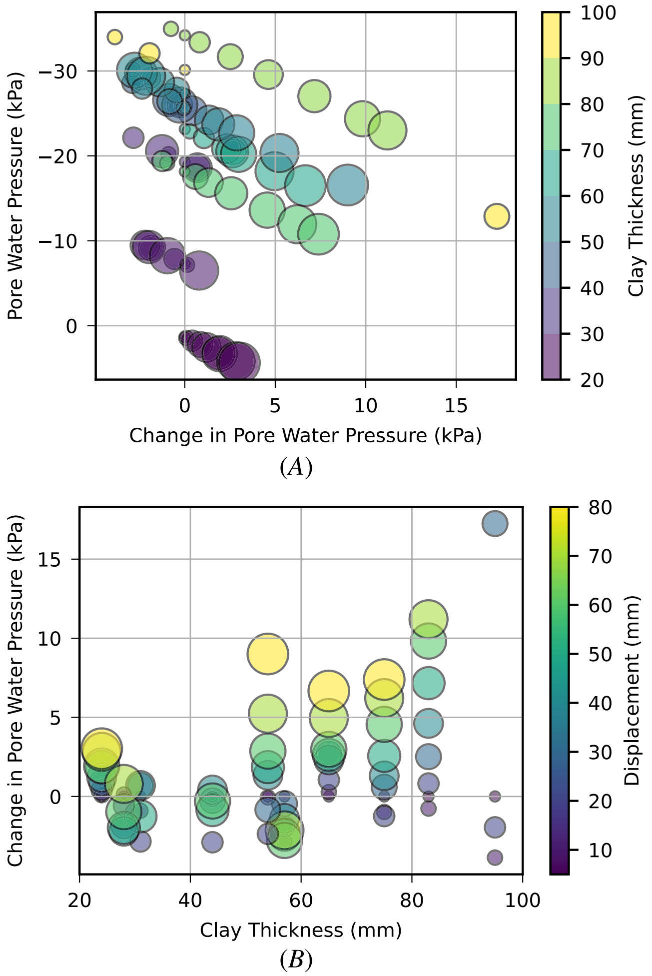

TABLE 2

Pore water pressure (suction) measured and derived parameters

				Values at 50-mm Mutual Displacement		
Clay Thickness, mm	Initial Suction, kPa	Final Suction, kPa	Δu_s, kPa	RMS_s, kPa	C_s, kPa·s	CA_{sc}, kPa
24	0.45	4.22	3.77	1.15	1,780.80	6.96
28	−7.07	−6.74	0.33	1.43	6,610.91	13.71
31	−19.06	−20.73	−1.67	0.64	19,543.25	23.64
44	−18.82	−26.83	−8.01	7.22	33,254.52	43.86
54	−20.10	−17.27	2.83	5.51	18,919.95	56.99
57	−24.08	−30.10	−6.02	4.34	16,115.37	45.28
65	−23.61	−16.14	7.47	2.12	20,032.65	21.05
75	−17.52	−11.06	6.46	0.89	17,206.04	25.41
83	−35.87	−22.29	13.58	4.11	29,692.90	26.02
95	−32.77	−19.22	13.55	…	…	…

remarkable for thicker specimens (clay plates with a thickness of 83 and 95 mm), where only low displacement amplitudes could be applied.

Figure 13*B* illustrates the change in suction, where an increase in values indicates reduced suction levels, whereas a decrease suggests a further increase in suction. In general, specimens thinner than 60 mm embody increasing levels of suction during the test and mostly remain at a net suction state as tabulated by their final suction and suction difference values in Table 2. This is especially true for clay plates with thicknesses of 31, 44, and 57 mm, where the pore water pressure regime remains in suction state, which means that the specimen retains a higher suction value than its initial value. For thicker plates, the general tendency is pore water pressure relaxation where reduced suction amplitudes are recorded at the end of the test. It is plausible that the larger structural rigidity of thicker clays could suppress further suction buildup. It is also possible that the large clay volume might allow for partial dissipation of pore water pressure within the specimen geometry, which is less likely to occur in thinner specimens. Table 2 also presents additional parameters used to characterize the suction regime. A reference displacement level of 50 mm, which is termed mutual displacement, is selected in this table to enable consistent comparison of the various suction metrics. Since the tests are conducted independently, a common displacement level is used for comparing the suction metrics. These additional parameters are listed as follows:

1. Initial suction captures the starting pore water pressure in the clay, which shows the initial stress state.
2. Final suction indicates the residual state of the pore water pressure and shows the progression of the overall regime.
3. Change in suction (Δu_s) is used to quantify the change of suction between initial and final states, which serves to show how clay reacts to bending in terms of pore pressure regime.
4. Root mean square suction (RMS_s) indicates the variability of pore water pressure readings during the test. Figure 14 illustrates the baseline corrected (zeroed) RMS_s parameter, which shows the global trends in the suction regime. Although the parameter itself is by definition always positive, specimens with thicknesses of 65, 83, and 95 mm exhibit a net reduction trend in the suction values, which is reflected as a decreasing trend in the baseline corrected plots. RMS_s is calculated as follows:

$$RMS_s = \sqrt{\frac{1}{N}\sum_{i=1}^{N}[u_{si}]^2} \tag{2}$$

5. Cumulative suction (C_s) illustrates the total suction embodied in the clay over the duration of the test. Figure 15 illustrates the evolution of this parameter in displacement domain. It is expressed in the following form:

FIG. 14

Baseline corrected root mean square suction (RMS_s) plots for the tests. Red shaded region shows where suction reduces.

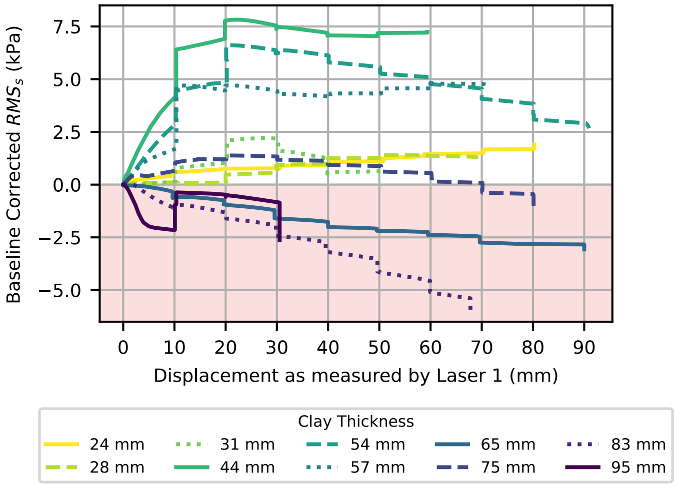

FIG. 15

Plots of cumulative suction (C_s) parameter as a function of displacement. Note that the values of clays with a thickness of 65, 83, and 95 mm are inverted in accordance with their overall trend shown in **Figure 14**.

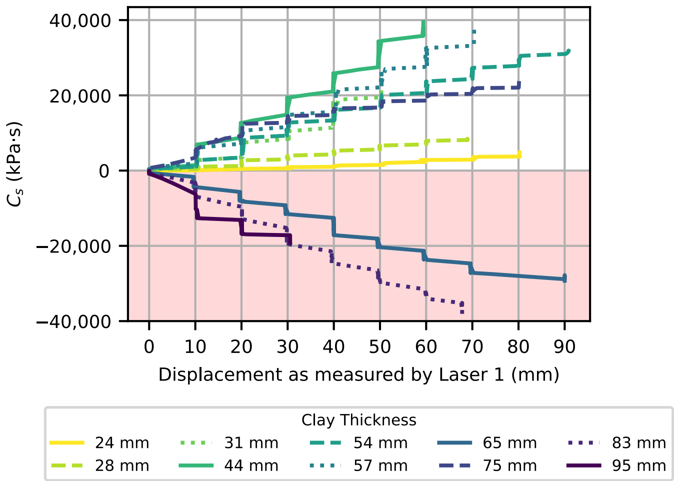

$$C_s = \sum_{i=1}^{N} [u_{si} \cdot \Delta t_i] \quad (3)$$

6. Cumulative absolute suction change is a parameter that was inspired by the cumulative absolute velocity intensity measure used in earthquake geotechnics (Campbell and Bozorgnia 2010). This parameter shows the cumulative intensity of the pore water pressure fluctuations by summing the pore water changes, and it is thought that these fluctuations or their cumulative effects could be driving clay cracking. Larger values of the parameter are indicative of significant pore water pressure fluctuations, which could drive crack propagation and material degradation. **Figure 16** shows the evolution of the cumulative derivatives of suction changes in displacement domain. The parameter is expressed in the following manner in discretized form:

FIG. 16

Plots of cumulative absolute suction change (CA_{sc}) parameter in displacement domain. Note that the values of clays with a thickness of 65, 83, and 95 mm are inverted in accordance with their overall trend shown in **Figure 14**.

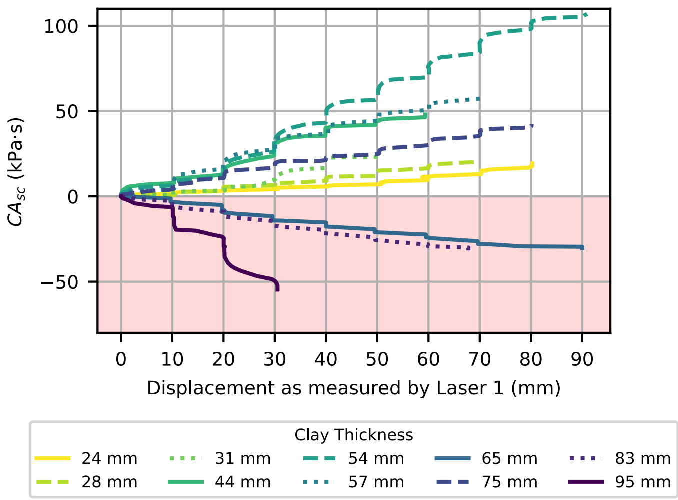

$$CA_{sc} = \sum_{i=1}^{N-1} \left| u_{s_{i+1}} - u_{s_i} \right| \tag{4}$$

Based on the analysis of the suction regimes and the associated parameters, it is seen that some of the clay plates exhibit high levels of suction increase during the test. For instance, clays with a thickness of 44 and 57 mm show high values of across all metrics tabulated in **Table 2**. In the subsequent sections, it will be shown that these specimens have experienced a markedly high cracking. It will also be shown that different suction regimes, as determined by the parameters defined above, dictate the cracking trends in the clay plate. Particularly RMS_s and CA_{sc}, provide a unique way to quantify suction variability and cumulative effects of suction, which might offer unique insights into the mechanisms driving cracking. Finally, the following deductions can be made about the pore water pressure regime in the specimens tested:

1. At the onset of the tests, thicker plates embody larger suction pressure despite being unloaded at the same overburden stress as the thinner plates as seen from **Table 2**.
2. In terms of pore water pressures, overall variance in thicker clay plates is larger and the suction regime is the form of relaxation of pore water pressures.
3. At the onset of testing, in general, thinner clay plates start with lower suction pressures, but as the bending is progressed, the suction values increase appreciably.

CURVATURE AND CRACKING BEHAVIOR

Curvature is a key factor in understanding material response under flexure, and its utility in defining moment-curvature relationships has significant practical applications. Given the significance of moment-curvature relationships for practical applications, in this study, 3D scan data are used to directly capture curvature. Additionally, curvature has been analytically calculated using the beam theory assumptions applied to the bending of compacted landfill covers by Gourc et al. (2010). These assumptions estimate the radius of maximum curvature (R) and bending strain ε_b with the following expressions:

$$R = \left(\frac{a}{2} - \frac{l^2}{8a} \right) \tag{5}$$

$$\varepsilon_b = R_{\mathrm{NI}} \kappa d \qquad (6)$$

where a and l are the vertical displacement and length of the element. R_{NI} is the ratio of the distance between the top of the element and the neutral axis and the depth of the element and κ is the curvature $(1/R)$, and d is the thickness of the clay. Figure 17 illustrates the comparison between the measured curvature as extracted from 3D scan data and analytical curvature calculations. Although a reasonably good fit with a coefficient of determination of nearly 0.8 is observed, slight deviations are seen for thicker clay plates. This might stem from the application of beam theory to high-thickness elements where nonlinearities in material behavior and stress distribution might affect the results.

Although studies delving into the bending behavior of compacted clays indicate that crack initiation occurs at relatively low strain levels (Camp, Gourc, and Ple 2010; Li et al. 2022), when clay is consolidated from slurry at relatively high water contents, the cracking initiation occurs at higher strains. Specifically, whereas Gourc et al. (2010) and Li et al. (2022) indicate crack initiation strains as low as 0.6 % and 0.5 %, Thusyanthan et al. (2007) report strain values in the order of 2–4 % for crack initiation. The initial scanning of the clay surfaces at a vertical displacement of 10 mm at a strain of approximately 3–4 %, fit within the crack initiation strains outlined by Thusyanthan et al. (2007). Moreover, since the focal point of the current study is the large deformation behavior of clay plates, detection of crack initiation is not explicitly studied in detail.

Figure 18*A* illustrates the evolution of curvature at different displacement levels, and figure 18*B* shows how cracked area percentages increase with curvature. In figure 18*B*, it is seen that there is a threshold curvature value of approximately 0.003 mm^{-1} beyond which almost all of the specimens tested show a pronounced increase in the percentage of the cracked area. Beyond the induced curvature, another contributing factor to the cracking of the clay is the pore water pressure regime, which is not immediately visible in figure 18. Although the plots in figure 18 do not show the effects of suction on the cracked percentage, Table 2 tabulates the parameters, which quantify the suction. Specimens with thicknesses of 57, 44, and 31 mm exhibit marked cracking behavior at early stages of curvature values. The tabulated values of suction parameters such as RMS_s, C_s, and CA_{sc} are also among the highest for these specimens.

Figure 19 illustrates the interplay between the curvature of the clay plates and the cumulative suction (C_s), where it is seen that in order to attain a given curvature value, a larger accumulation of pore water pressure is

FIG. 17

Measured versus analytical curvature.

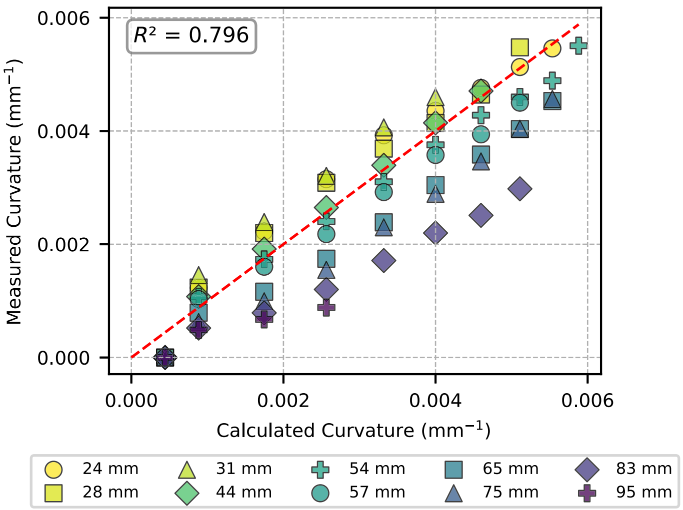

FIG. 18

Relationships among curvature, displacement, and cracking for the clay plates: (*A*) corrected displacement versus curvature; (*B*) curvature versus percentage of cracked area.

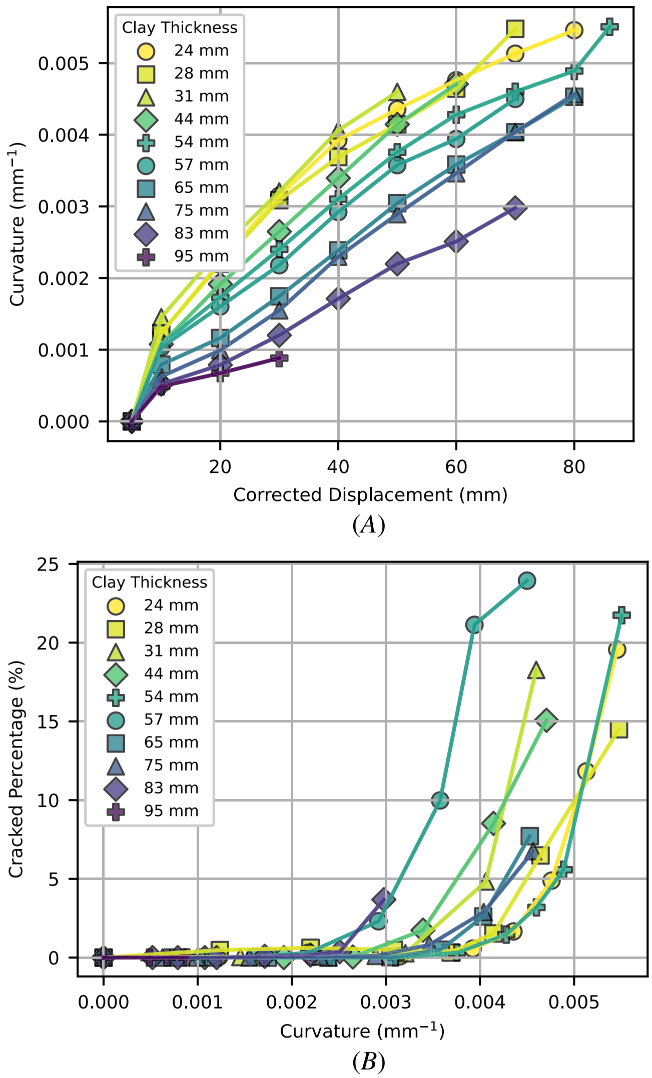

needed. In other words, for a given amount of bending, thicker clay specimens generate higher cumulative suction in comparison to thinner specimens. This indicates that stiffer clay plates might embody larger suction levels as bending progresses. These trends also show that thicker specimens possess a larger capacity to retain suction than thin specimens that are under the same curvature level. In general, parameters such as RMS_s, C_s, and CA_{sc} can be used in predicting the cracking of clay specimens as the values of these parameters for excessively cracked specimens are markedly higher than specimens undergoing minimal cracking.

Although the C_s indicates how the suction is generated in a clay plate, it does not totally explain the cracking behavior. RMS_s parameter captures the cracking trends more accurately, as it also accounts for not only the cumulative suction value but also the changes in the suction regime. **Figure 20** illustrates a 3D plot relating curvature, RMS_s, and cracked percentage where a complex interaction can be observed. According to the trends depicted in **figure 20**, there are two regimes in which the clay can undergo beyond the threshold value of the curvature (0.003 mm^{-1} as explained above):

FIG. 19 Plots of curvature versus cumulative suction (C_s) for all tests.

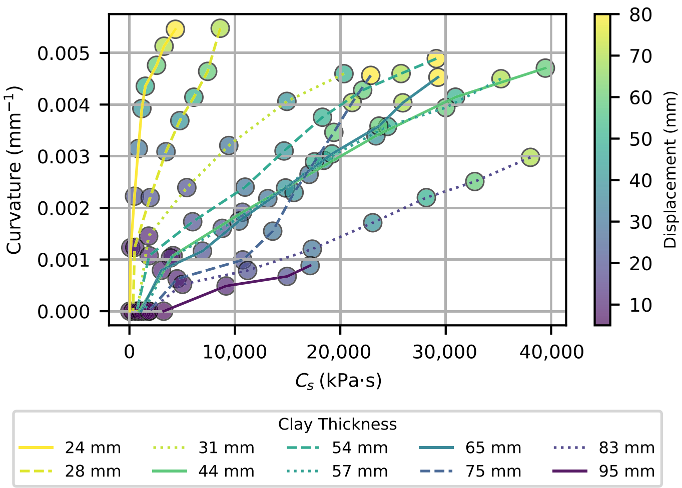

(1) If the pore water pressure regime as defined by RMS_s starts decreasing, the cracking progress at a much lower rate as indicated by the slopes of the curves that tilt toward the upper-right-hand side in figure 20. For instance, this trend is seen in clay plate with a thickness of 54 mm.

(2) If the value of RMS_s does not decrease beyond the threshold curvature value, the cracking occurs at an elevated rate where significant cracking is observed in the plates with increasing curvature. An example behavior with this trend is observed in the behavior of 44-mm-thick clay plate in figure 20.

FIG. 20 3D plot indicating the interplay between curvature, suction regime, and cracking.

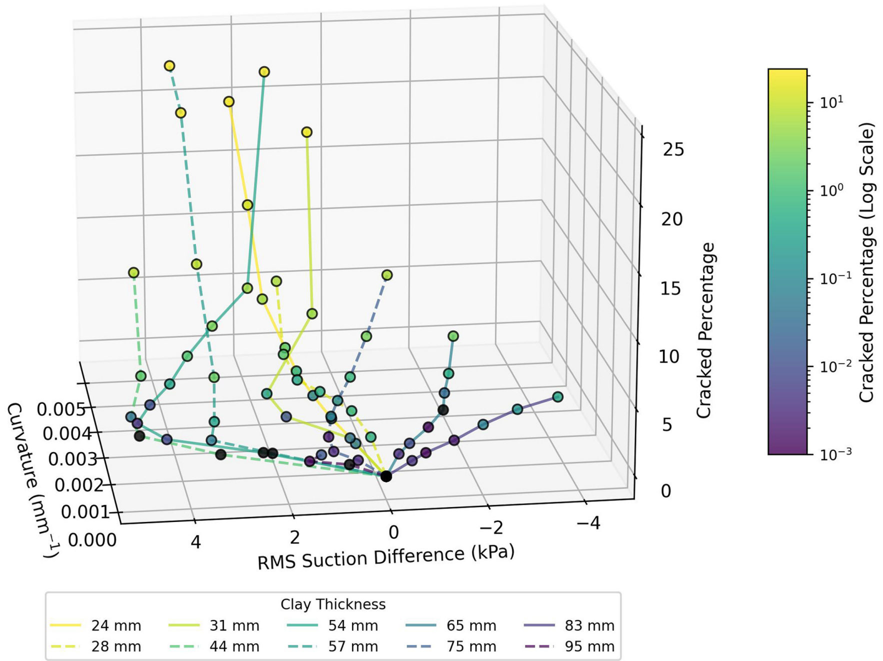

TABLE 3
Thickness normalized parameters of pore water pressure (suction)

Clay Thickness, mm	Curvature at 5 % Cracked Area, mm^{-1}	Cracked % at 0.004 Curvature	Ultimate State Cracked %
24	0.004763084	0.80	19.55
28	0.004395307	0.88	14.50
31	0.004068159	3.99	18.26
44	0.003713238	6.96	15.07
54	0.004808791	0.87	21.74
57	0.003116648	21.66	23.93
65	0.004265432	2.47	7.71
75	0.004321327	2.76	6.75
83	NA	NA	3.68
95	NA	NA	0.01

Table 3 illustrates the cracked percentages of clays specimens, and it is seen that at a reference curvature of 0.004 mm^{-}, these two specimens had the highest amount of cracked area. Table 3 also tabulates the curvature of the plates at 5 % cracking and ultimate cracked percentages. Using Table 3 for comparing the 54- and 57-mm-thick specimens also reveals key insights. Although these clay plates are seemingly similar in thickness, their response was markedly different during the course of the tests where 57-mm-thick specimen showed an earlier crack growth. One of the differences between the two specimens was the initial suction value that was slightly higher for the 57-mm specimen, which might explain the early crack growth. The increased value of suction likely facilitated crack initiation by increasing tensile stresses at critical points in 57-mm-thick specimen. Conversely, the relaxation regime in the 54-mm specimen in terms of RMS_s values as depicted in figure 14 might have delayed cracking and allowed for a more distributed stress state. The 54-mm-thick specimen exhibited a suction-relaxation-type behavior throughout the test, which resulted in the test being conducted to a higher displacement level than normal, and the large values of cracking percentages were only reached after 80 mm of displacement was exceeded as seen in figure 18. Therefore, it could be said that the initial suction value and the overall suction regime has a pronounced impact on the cracking behavior of clays.

Another specimen that showed an early increase in the cracked percentage is a 44-mm-thick clay plate. This specimen had the highest increase in suction value at the end of the test with an added suction pressure of approximately 8 kPa by the end of the test as seen in Table 2. Similarly, the values of RMS_s, C_s, and CA_{sc} parameters were the highest or among the highest for this specimen. Consequently, an early increase in the cracked percentage increase is seen in this specimen, and the overall trend in the 3D space illustrated in figure 20 show an upper-right-hand trend, which is associated with large cracked percentages. The RMS_s values were sustained at a plateau for this specimen before the onset of cracking.

BENDING MOMENTS

Once the deformed geometry of the clay plates were rendered into usable information in terms of bending curvatures and cracking percentages, the moment-curvature relationship could be calculated. In order to account for the side friction, the lateral friction was subtracted from the applied stress with membrane correction in the following manner:

$$\sigma_{bending} = \sigma_{corr} - \frac{\tau_{interface}}{A_{plate}} \tag{7}$$

The expression above is in similar form to equation (1), but here, the pore water pressures developing inside the specimen are considered as internal forces and consequently they are not directly incorporated in the formulation. $\sigma_{bending}$ is solely the external bending effort applied onto the specimen, which is assumed to be

FIG. 21

Bending moment per unit length versus curvature plots for all specimens.

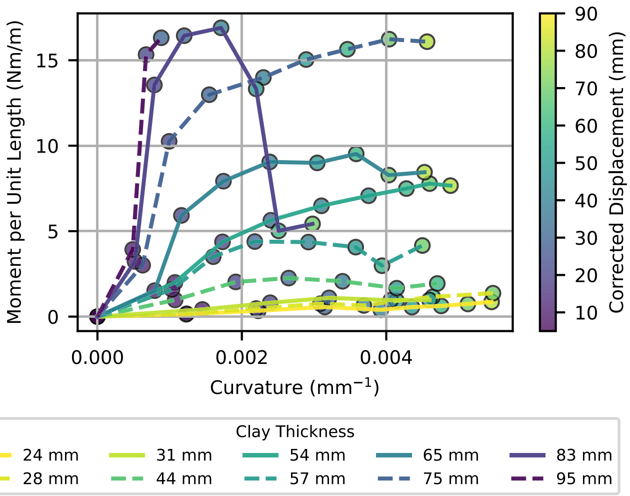

undergoing pure bending conditions. Timoshenko (1959) approximates the bending moment per unit length of a circular plate under pure bending in the following form:

$$M = \sigma_{bending} \cdot \frac{h^2}{6} \tag{8}$$

where h is the thickness of the plate. Based on the formulation above, **figure 21** illustrates the curvature versus bending moment per unit length of the clay specimens. The plots in **figure 21** start from zero curvature values and then continue on with the back-calculated curvature values from the image analysis. As it was not possible to acquire curvature values continuously due to intermediate scanning of the clay surface and curvature data prior to the first scan are not available, the plots were zeroed to start at the first measured curvature point for all specimens. In line with this approach, the bending moments were also initialized at zero, which allows for a comparable comparison of how moment resistance develops in each specimen. **Figure 21** shows that clay thickness or the overall sectional stiffness determines the bending moment the specimen can withstand. It is also seen that the thicker specimens exhibit a more brittle behavior than thinner specimens. It must be noted that the 83- and 95-mm specimens tumbled and further continuation of testing was not possible. Therefore, these specimens were only tested to lower displacement values. This also explains the significant reduction in the capacity of 83-mm-thick clay specimen as the cracked percentage in this specimen does not go beyond 5 %.

Discussion

The experimental results presented herein provide new insights into the flexural and cracking behavior of clay plates under bending conditions. The innovative testing framework introduced in this study enables a more controlled means of experimentally determining the bending and cracking behavior of clays. The experimental design also minimizes the influence of self-weight and point loading effects (stress concentrations) that are commonly encountered in conventional beam and burst-type tests. The findings demonstrate that the bending and cracking response of clay is significantly influenced by the pore water pressure regime, and the newly proposed suction parameters offer new insights to quantify the behavior of the clay. This study has also identified a curvature threshold for crack initiation, which is approximately 0.003 mm^{-1}, and this level of curvature can provide a practical benchmark for evaluating flexural resistance in various geotechnical applications. The applicability of these results will be the subject of subsequent studies by the authors.

It is acknowledged that while the experimental findings contribute to a better understanding of clay bending and cracking mechanisms, there are inherent limitations associated with the tests presented herein. For example, the pore water pressure measurements were conducted at the periphery of the specimen, and an implicit assumption was made that these values are representative of the entirety of the clay plate. It is possible that spatial variations in pore pressure distribution exists within the specimen. This is especially true near the crack initiation zones, and this might influence the measured suction response. Future experimental studies should consider additional sensor placements, specimen sizes, and geometries. It is also envisaged that the effects of wetting-drying cycles will be included as a part of the subsequent research endeavors. Beyond physical modelling, the authors will use numerical models with constitutive models of appropriate complexity. The numerical models will initially aim to replicate the experimental conditions and provide a more detailed assessment of stress distribution, suction effects, and fracture propagation within the clay plates. It is also foreseen that once the numerical models' predictive capabilities are validated with experimental data, the models will also be used for parametric studies on different clay types, boundary conditions, and loading rates to shed light on the behavior of wider range of infrastructure assets.

The practical implications of this study are significant for infrastructure systems where clay materials are integral to structural stability or to the function of an infrastructure asset, which might include landfill covers, embankments, and dike engineering. The results from this study can be used to refine design criteria for clay cover layers subjected to flexural loading, improve risk assessment models for crack-induced permeability changes, and inform maintenance strategies for flood defense systems. The developed parameters for suction regime can be incorporated into field monitoring campaigns' data analysis methods to give rise to resilient geotechnical structures under varying environmental and loading conditions.

Conclusions

Clays or clay cover layers play an important role in safeguarding critical infrastructure assets such as dikes, dams, and waste storage facilities. This study presented an innovative testing framework for determination of bending and cracking behavior of clays plates. Key findings of this study can be concluded as follows:

- This study introduced a novel experimental setup using an inflatable membrane to apply pure bending conditions on clay plates, which addresses the limitations in traditional beam and burst tests. This technique might have the potential to become a unified testing method for bending and cracking resistance determination of clays.
- The cracking of the clay plates was driven by the changes in the suction regime within the specimen. Beyond the conventional description of the suction pressure, this study has defined a set of new parameters that help to explain the observed cracking behavior of clay plates. These parameters include RMS_s, C_s, and CA_{sc}.
- It is also seen that thicker clay plates generally exhibit a higher initial suction value, but these specimens tend to undergo suction relaxation as the bending is continued. Thinner specimens, however, can exhibit significant suction build-up during bending, which increases their cracking potential.
- The bending tests yielded a curvature threshold for cracking of the clay plates tested in this study. According to this, a curvature threshold of approximately 0.003 mm^{-1} was identified as the limit beyond which clay plates showed a marked increase in the cracked area percentage. This limit was observed for almost all of the specimens tested.
- Despite the methodological differences, the consolidation stress normalized bending stress values in the present study showed reasonable agreement with a four-point bending study conducted earlier. The fit was especially good for small displacement measurements. However, as this study focused on large deformations, the agreement diminished at higher displacements, which is most likely due to the nonlinear and second-order effects associated with large deformation behavior. The clay plates tested herein have had

significantly large portions of their surface areas cracked. The cracked area expressed as a percentage was as large as 21 % in some cases.

- The novel parameters defining the suction regime in clays were prescribed in this study. The utility of these parameters in explaining the cracking behavior was also elaborated. These parameters can potentially be used in field-monitoring campaigns to provide early warnings of cover layer deterioration. These parameters could be integrated into analysis of data emanating from flood defenses, dikes, and landfill caps to predict cracking risks and optimize maintenance strategies.

References

Al-Tabbaa, A. and D. M. Wood. 1987. "Some Measurements of the Permeability of Kaolin." *Géotechnique* 37, no. 4 (December): 499–514. https://doi.org/10.1680/geot.1987.37.4.499

Aliha, M. R. M., H. G. Kouchaki, and P. J. Haghighatpour. 2023. "Designing a Simple and Suitable Laboratory Test Specimen for Investigating the General Mixed Mode I/II/III Fracture Problem." *Materials & Design* 236: 112477. https://doi.org/10.1016/j.matdes.2023.112477

Andersen, K. H., C. G. Rawlings, T. A. Lunne, and T. H. By. 1994. "Estimation of Hydraulic Fracture Pressure in Clay." *Canadian Geotechnical Journal* 31, no. 6 (December): 817–828. https://doi.org/10.1139/t94-099

Atkinson, J. H., 1994. "Undrained Hydraulic Fracture in Cavity Expansion Tests." In *Proceedings of the 13th International Conference on Soil Mechanics and Foundation Engineering*, 1009–1012. London: International Society for Soil Mechanics and Geotechnical Engineering.

Bjerrum, L., J. K. T. L. Nash, R. M. Kennard, and R. E. Gibson. 1972. "Hydraulic Fracturing in Field Permeability Testing." *Géotechnique* 22, no. 2 (June): 319–332. https://doi.org/10.1680/geot.1972.22.2.319

Camp, S., O. Plé, and J. P. Gourc. 2009. "Proposed Protocol for Characterizing a Clay Layer Subjected to Bending." *Geotechnical Testing Journal* 32, no. 3 (May): 273–279. https://doi.org/10.1520/GTJ101438

Camp, S., J. P. Gourc, and O. Ple. 2010. "Landfill Clay Barrier Subjected to Cracking: Multi-scale Analysis of Bending Tests." *Applied Clay Science* 48, no. 3 (April): 384–392. https://doi.org/10.1016/j.clay.2010.01.011

Campbell, K. W. and Y. Bozorgnia. 2010. "A Ground Motion Prediction Equation for the Horizontal Component of Cumulative Absolute Velocity (CAV) Based on the PEER-NGA Strong Motion Database." *Earthquake Spectra* 26, no. 3 (August): 635–650. https://doi.org/10.1193/1.3457158

Cengiz, C. and E. Güler. 2018. "Seismic Behavior of Geosynthetic Encased Columns and Ordinary Stone Columns." *Geotextiles and Geomembranes* 46, no. 1 (February): 40–51. https://doi.org/10.1016/j.geotexmem.2017.10.001

Cengiz, C., M. Cabrera, B. Wittekoek, M. Fransen, L. Wopereis, and C. Zwanenburg. 2024. "Centrifuge Tests on the Uplift and Deformation Patterns of Clay Cover Layers in Deltas." In *Geotechnical Engineering Challenges to Meet Current and Emerging Needs of Society*, 1052–1055. Boca Raton, FL: CRC Press.

Chandler, H. W. 1984. "The Use of Non-linear Fracture Mechanics to Study the Fracture Properties of Soils." *Journal of Agricultural Engineering Research* 29, no. 4 (June): 321–327. https://doi.org/10.1016/0021-8634(84)90087-8

Chum, O. and J. Matas. 2008. "Optimal Randomized RANSAC." *IEEE Transactions on Pattern Analysis and Machine Intelligence* 30, no. 8 (August): 1472–1482. https://doi.org/10.1109/TPAMI.2007.70787

Construction Industry Research and Information Association (CIRIA). 2013. *The International Levee Handbook*. London: CIRIA.

Decker, R. A. and S. P. Clemence. 1981. "Laboratory Study of Hydraulic Fracturing in Clay." In *Proceedings of the 10th Internatiaonal Conference on Soil Mechanics and Foundation Engineering*, Vol. 1, 573–575. Rotterdam, the Netherlands: Balkema.

Divya, P. V., B. V. S. Viswanadham, and J. P. Gourc. 2017. "Centrifuge Model Study on the Performance of Fiber Reinforced Clay-Based Landfill Covers Subjected to Flexural Distress." *Applied Clay Science* 142: 173–184. https://doi.org/10.1016/j.clay.2016.12.010

Fischler, M. A. and R. C. Bolles. 1981. "Random Sample Consensus: A Paradigm for Model Fitting with Applications to Image Analysis and Automated Cartography." *Communications of the ACM* 24, no. 6 (June): 381–395. https://doi.org/10.1145/358669.358692

Frikha, W., M. Bouassida, and J. Canou. 2013. "Observed Behaviour of Laterally Expanded Stone Column in Soft Soil." *Geotechnical and Geological Engineering* 31, no. 2 (April): 739–752. https://doi.org/10.1007/s10706-013-9624-8

Fukushima, S. 1986. "Hydraulic Fracturing Criterion in the Core of Fill Dams" (in Japanese). *Report of Fujita Kogyo Technical Institute* 22: 131–136.

Gössling, S., C. Neger, R. Steiger, and R. Bell. 2023. "Weather, Climate Change, and Transport: A Review." *Natural Hazards* 118, no. 2 (September): 1341–1360. https://doi.org/10.1007/s11069-023-06054-2

Gourc, J. P., S. Camp, B. V. S. Viswanadham, and S. Rajesh. 2010. "Deformation Behavior of Clay Cap Barriers of Hazardous Waste Containment Systems: Full-Scale and Centrifuge Tests." *Geotextiles and Geomembranes* 28, no. 3 (June): 281–291. https://doi.org/10.1016/j.geotexmem.2009.09.014

Hallett, P. D. and T. A. Newson. 2001. "A Simple Fracture Mechanics Approach for Assessing Ductile Crack Growth in Soil." *Soil Science Society of America Journal* 65, no. 4 (July): 1083–1088. https://doi.org/10.2136/sssaj2001.6541083x

Jamalinia, E., P. J. Vardon, and S. C. Steele-Dunne. 2020. "The Impact of Evaporation Induced Cracks and Precipitation on Temporal Slope Stability." *Computers and Geotechnics* 122: 103506. https://doi.org/10.1016/j.compgeo.2020.103506

Jaworski, G. W., J. M. Duncan, and H. B. Seed. 1981. "Laboratory Study of Hydraulic Fracturing." *Journal of the Geotechnical Engineering Division* 107, no. 6 (June): 713–732. https://doi.org/10.1061/AJGEB6.0001147

Lau, B. H. "Cyclic Behaviour of Monopile Foundations for Offshore Wind Turbines in Clay." PhD diss., University of Cambridge, 2015.

Leonards, G. A. and J. Narain. 1963. "Flexibility of Clay and Cracking of Earth Dams." *Journal of the Soil Mechanics and Foundations Division* 89, no. 2 (March): 47–98. https://doi.org/10.1061/JSFEAQ.0000504

Li, H.-D., C.-S. Tang, Q. Cheng, S.-J. Li, X.-P. Gong, and B. Shi. 2019. "Tensile Strength of Clayey Soil and the Strain Analysis Based on Image Processing Techniques." *Engineering Geology* 253: 137–148. https://doi.org/10.1016/j.enggeo.2019.03.017

Li, H.-J., H.-H. Zhu, C.-X. Zhang, N. G. Reddy, A. Garg, and H.-Y. Wu. 2022. "Monitoring Flexure Behavior of Compacted Clay Beam Using High-Resolution Distributed Fiber Optic Strain Sensors." *Geotechnical Testing Journal* 45, no. 3 (May): 627–643. https://doi.org/10.1520/GTJ20200331

Liu, Z., Z. Han, L. Qin, D. Cao, C. Guo, F. Wang, B. Ma, and J. Wu. 2023. "Identification of Bending Fracture Characteristics of Cement-Stabilized Coral Aggregate in Four-Point Bending Tests Based on Acoustic Emission." *Construction and Building Materials* 402: 132999. https://doi.org/10.1016/j.conbuildmat.2023.132999

Lo, K. Y. and K. Kaniaru. 1990. "Hydraulic Fracture in Earth and Rock-Fill Dams." *Canadian Geotechnical Journal* 27, no. 4 (August): 496–506. https://doi.org/10.1139/t90-064

Marchi, M., G. Gottardi, and K. Soga. 2014. "Fracturing Pressure in Clay." *Journal of Geotechnical and Geoenvironmental Engineering* 140, no. 2 (February): 04013008. https://doi.org/10.1061/(ASCE)GT.1943-5606.0001019

Mori, A. and M. Tamura. 1987. "Hydrofracturing Pressure of Cohesive Soils." *Soils and Foundations* 27, no. 1 (March): 14–22. https://doi.org/10.3208/sandf1972.27.14

Murugesan, S. and K. Rajagopal. 2010. "Studies on the Behavior of Single and Group of Geosynthetic Encased Stone Columns." *Journal of Geotechnical and Geoenvironmental Engineering* 136, no. 1 (January): 129–139. https://doi.org/10.1061/(ASCE)GT.1943-5606.0000187

Panah, A. K. and E. Yanagisawa. 1989. "Laboratory Studies on Hydraulic Fracturing Criteria in Soil." *Soils and Foundations* 29, no. 4 (December): 14–22. https://doi.org/10.3208/sandf1972.29.4_14

Plé, O., A. Manicacci, J. P. Gourc, and S. Camp. 2012. "Flexural Behaviour of a Clay Layer: Experimental and Numerical Study." *Canadian Geotechnical Journal* 49, no. 4 (April): 485–493. https://doi.org/10.1139/t2012-006

Rossato, G., N. Ninis, and R. Jardine. 1994. "On Stress-Strain and Strength Properties of Model Soils." In *Proceedings of the 13th International Conference on Soil Mechanics and Foundation Engineering*, 389–392. London: International Society for Soil Mechanics and Geotechnical Engineering.

Smith, M. G. "A Laboratory Study of the Marchetti Dilatometer." PhD diss., Oxford University, 1993.

Tang, C.-S., X.-J. Pei, D.-Y. Wang, B. Shi, and J. Li. 2015. "Tensile Strength of Compacted Clayey Soil." *Journal of Geotechnical and Geoenvironmental Engineering* 141, no. 4 (April): 04014122. https://doi.org/10.1061/(ASCE)GT.1943-5606.0001267

Tang, J., C. Guo, L. Qin, H. Wang, F. Shi, Z. Liu, L. Pei, and J. Liu. 2024. "Fracture Characteristics of Cement-Stabilized Macadam Using Three-Point Bending Test." *Construction and Building Materials* 419: 135384. https://doi.org/10.1016/j.conbuildmat.2024.135384

Thusyanthan, N. I., W. A. Take, S. P. G. Madabhushi, and M. D. Bolton. 2007. "Crack Initiation in Clay Observed in Beam Bending." *Géotechnique* 57, no. 7 (September): 581–594. https://doi.org/10.1680/geot.2007.57.7.581

Timoshenko, S. 1959. *Theory of Plates and Shells*. New York: McGraw-Hill.

Tsubakihara, Y. and H. Kishida. 1993. "Frictional Behaviour between Normally Consolidated Clay and Steel by Two Direct Shear Type Apparatuses." *Soils and Foundations* 33, no. 2 (June): 1–13. https://doi.org/10.3208/sandf1972.33.2_1

Tsubakihara, Y., H. Kishida, and T. Nishiyama. 1993. "Friction between Cohesive Soils and Steel." *Soils and Foundations* 33, no. 2 (June): 145–156. https://doi.org/10.3208/sandf1972.33.2_145

Van, M. A., A. R. Koelewijn, and F. B. Barends. 2005. "Uplift Phenomenon: Model, Validation, and Design." *International Journal of Geomechanics* 5, no. 2 (June): 98–106. https://doi.org/10.1061/(ASCE)1532-3641(2005)5:2(98)

van der Krogt, M. G., T. Schweckendiek, and M. Kok. 2021. "Improving Dike Reliability Estimates by Incorporating Construction Survival." *Engineering Geology* 280: 105937. https://doi.org/10.1016/j.enggeo.2020.105937

Vardon, P. J. 2015. "Climatic Influence on Geotechnical Infrastructure: A Review." *Environmental Geotechnics* 2, no. 3 (June): 166–174. https://doi.org/10.1680/envgeo.13.00055

Vu, T. M. and A. K. Mishra. 2019. "Nonstationary Frequency Analysis of the Recent Extreme Precipitation Events in the United States." *Journal of Hydrology* 575: 999–1010. https://doi.org/10.1016/j.jhydrol.2019.05.090

Wang, J.-J., J.-G. Zhu, C. F. Chiu, and H. Zhang. 2007. "Experimental Study on Fracture Toughness and Tensile Strength of a Clay." *Engineering Geology* 94, nos. 1-2 (October): 65–75. https://doi.org/10.1016/j.enggeo.2007.06.005

Wang, J., S. Huang, W. Guo, Z. Qiu, and K. Kang. 2020. "Experimental Study on Fracture Toughness of a Compacted Clay Using Semi-circular Bend Specimen." *Engineering Fracture Mechanics* 224: 106814. https://doi.org/10.1016/j.engfracmech.2019.106814

Zervos, A., P. Papanastasiou, and I. Vardoulakis. 2008. "Shear Localisation in Thick-Walled Cylinders under Internal Pressure Based on Gradient Elastoplasticity." *Journal of Theoretical and Applied Mechanics* 38, nos. 1-2: 81–100.

Zhang, G., R. Wang, J. Qian, J.-M. Zhang, and J. Qian. 2012. "Effect Study of Cracks on Behavior of Soil Slope under Rainfall Conditions." *Soils and Foundations* 52, no. 4 (August): 634–643. https://doi.org/10.1016/j.sandf.2012.07.005

Zwanenburg, C., B. Witteloek, M. Martinelli, E. Alderlieste, and R. Zwaan. 2023. "Calibration Chamber for Numerical Tools (Version 1)." Zenodo. https://doi.org/10.5281/zenodo.8066899

Zwanenburg, C., C. Cengiz, M. P. Fransen, B. Wittekoek, and L. Wopereis. 2024. "Testing Dike Stability under Uplift Conditions; An Experimental Study." In *Proceedings of the Fifth European Conference on Physical Modelling in Geotechnics*, 1–13. London: International Society for Soil Mechanics and Geotechnical Engineering. https://doi.org/10.53243/ECPMG2024-149